Ultrasound velocimetry in a shear-thickening wormlike micellar solution: Evidence for the coexistence of radial and vorticity shear bands

V. Herle[1,a], S. Manneville[2], and P. Fischer[1]

1 Institute of Food Science and Nutrition, ETH Zurich, 8092 Zurich, Switzerland
2 Ecole Normale Supérieure de Lyon, Laboratoire de Physique, 46 allée d'Italie, 69364 Lyon cedex 07, France

Abstract. We carried out pointwise local velocity measurements on 40 mM cetylpyridinium chloride-sodium salicylate (CPyCl-NaSal) wormlike micellar solution using high-frequency ultrasound velocimetry in a Couette shear cell. The studied wormlike solution exhibits Newtonian, shear-thinning and shear-thickening rheological behavior in a stress-controlled environment. Previous rheology, flow visualization and small-angle light/neutron scattering experiments in the shear-thickening regime of this system showed the presence of stress-driven alternating transparent and turbid rings or vorticity bands along the axis of the Couette geometry. Through local velocity measurements we observe a homogeneous flow inside the 1 mm gap of the Couette cell in the shear-thinning (stress-plateau) region. Only when the solution is sheared beyond the critical shear stress (shear-thickening regime) in a stress-controlled experiment, we observe inhomogeneous flow characterized by radial or velocity gradient shear bands with a highly sheared band near the rotor and a weakly sheared band near the stator of the Couette geometry. Furthermore, fast measurements performed in the shear-thickening regime to capture the temporal evolution of local velocities indicate coexistence of both radial and vorticity shear bands. However the same measurements carried out in shear rate controlled mode of the rheometer do not show such rheological complexity.

PACS. 83.80.Qr Surfactant and micellar systems, associated polymers – 83.60.Wc Flow instabilities – 47.50.-d Non-Newtonian fluid flows – 43.58.+z Acoustical measurements and instrumentation

1 Introduction

Addition of small amounts of counter-ions or co-surfactants to certain cationic surfactants leads to the formation of long threadlike or wormlike micelles [1]. Aqueous solutions of these wormlike micelles are viscoelastic and their rheological behavior has been widely studied during the past 20 years by several authors using many different experimental techniques [1–8]. The unique property of breakage and recombination of wormlike micelles and the large length scales in these systems induces a wide variety of complex structures under shear flow resulting in shear-induced structures (SIS) [9–15]. The formation of SIS in most cases is associated with shear bands, *i.e.* the formation of spatially inhomogeneous regimes. This leads to different stress or strain levels in the sheared solution and is expressed theoretically by a multi-branched constitutive equation [16–24]. In most cases the shear bands develop in the velocity gradient (or radial) direction in Couette

flow. However shear bands in the neutral (or vorticity) direction have also been observed for semi-dilute shear-thickening wormlike micellar solutions and are termed as vorticity bands [5,6,13,25,26]. Furthermore, both type of shear bands are usually transient in nature: in velocity gradient bands, the boundary between the bands moves radially and the vorticity bands undergo a flip-flop like change axially (see the video in Ref. [11] in [26]). This spatio-transient behavior of shear bands with different structures and hence different viscosities, manifests itself in oscillations of the overall rheological signals [8,13,27–30]. While many of the theoretical work address the formation of radial or velocity gradient shear bands [18,29,31], only a few attempts have been made towards explaining the vorticity bands [32–35].

In this article we focus on an equimolar (40 mM) mixture of cetylpyridinium chloride and sodium salicylate, a well-known surfactant-salt system that forms wormlike micelles in aqueous media [5–7,13]. Under linear flow conditions this particular solution behaves as a Maxwellian fluid with a single relaxation time, $\lambda = 0.02\,\mathrm{s}$, and a plateau modulus, $G_0 = 6.3\,\mathrm{Pa}$ [26]. However, the

a Present address: Ciba Inc., 4002 Basel, Switzerland; e-mail: vishwaherle@gmail.com

rheological response is very complex in the non-linear regime. At low shear stresses the solution initially shows Newtonian behavior followed by shear-thinning properties. At stresses beyond a critical stress, τ_c, the solution exhibits shear-thickening behavior. These rheological transitions are accompanied by the following optical behavior: i) at rest and in the Newtonian flow region the sample is optically transparent, ii) in the shear-thinning regime the entire solution turns slightly turbid, and iii) in the subsequent shear-thickening regime transparent and turbid rings suddenly appear in the vorticity (neutral) direction of the rheometer geometry [13,25,26]. These vorticity bands are observed in all standard rheometrical geometries, *i.e.*, in Couette, cone-plate and in parallel plate systems. In cone-plate and parallel plate geometries the bands appear as concentric rings [6,25] and in Couette geometry, they are stacked one above the other along the cylinder length [13,26]. A unique behaviour of these vorticity bands is that they alternate between their transparent and turbid states in a regular fashion. This leads to periodic oscillations in the shear rate ($\dot{\gamma}$), and apparent viscosity η, in stress-controlled experiments [25,26]. As long as the shear stress is kept constant ($\tau \geqslant \tau_c$) the bands continue to alternate and the material never reaches a stationary state [5,6,13,25,26]. Rheological, flow visualization and rheo small-angle light scattering studies of this system have indicated that these bands are stress-driven and the frequency of oscillations in $\dot{\gamma}$ and η are correlated to the frequency of appearance and disappearance of the bands, which is approximately 2 Hz. From rheo small-angle neutron scattering (SANS) measurements in the Newtonian and shear-thinning flow region it was shown that there was only a minor alignment of the wormlike micelles in the flow direction [26]. The anisotropic SANS intensity maps obtained from the triggered Rheo-SANS experiments and the anisotropy factor (A_f) calculated from the patterns indicated that both the oscillating transparent and turbid bands consist of highly anisotropic structures as compared to the structures in the shear-thinning regime with the turbid shear-thickening vorticity band having the highest anisotropy. Furthermore, by high-speed video imaging experiments we have also shown that the turbid band exhibits a high viscous flow response and that a phase shift ($\simeq \pi/2$) between the structural build up of the turbid band and the rheological response function results in the oscillation of the free rheological parameter ($f \simeq 2$ Hz) with the constant generation and destruction of the bands [26].

One of the aims of the present work is to verify the findings of the video imaging experiments by measuring the local viscosities in each vorticity band using ultrasound velocity profiling (UVP). UVP is a noninvasive velocimetric technique to measure local viscosities at microscopic resolutions inside the gap of rheometric geometry. This technique is based on time domain cross-correlation of high-frequency ultrasonic signals backscattered by tracer particles seeded in the flowing solution [36]. Figure 1a shows the typical linear velocity profile obtained by the UVP method for a Newtonian fluid being sheared in the gap of a Couette geometry. In this case the inner cylinder with radius
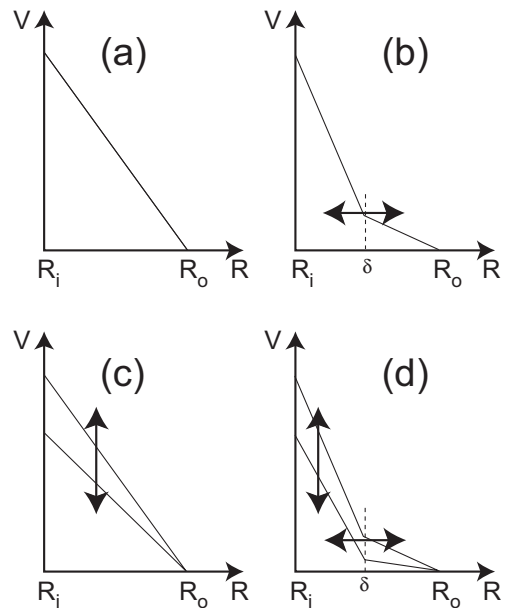
Fig. 1. Velocity profiles for (a) Newtonian fluid; (b) fluid showing radial shear bands; (c) fluid with vorticity banding; and (d) fluid showing both the radial and vorticity bands. R_i and R_o correspond to the radii of inner (rotating) and outer (stationary) cylinders of the Couette cell while δ is the boundary between the radial shear bands. The arrows indicate temporal fluctuations in the shear bands.

R_i is rotating while the outer cylinder of radius R_o is stationary. Hence the velocity is maximum at R_i and zero at R_o. However the situation is completely different for a solution forming radial shear bands in the gap. During such a shear banding flow condition, the sheared fluid separates into two differently sheared regions and consequently, in a Couette gometry, one observes a highly sheared band near the rotating cylinder (R_i) and a weakly sheared band at the stationary wall (R_o). Figure 1b shows a shear-banded velocity profile with the boundary of the band located at a distance δ from the rotating wall. Furthermore, if such a radial shear band is transient in nature, then this boundary will move within the gap of the Couette geometry as indicated by the horizontal arrow in Figure 1b. The system studied here, that is, 40 mM CPyCl-NaSal solution, shows vorticity bands which oscillate in the neutral direction. In that situation we expect the transient velocity profile to be similar to Figure 1c with the bands having different local viscosity during the flip-flop motion. The high and low viscous state at one spatial position at different observation times is represented by a low or higher shear rate, *i.e.*, velocity, V as indicated with lines in Figure 1c. The axial flip-flop motion of the bands is indicated by the vertical arrow. The readers are reminded here that such a situation can only occur when the shear stress is a commanded parameter and shear rate varies (or oscillates) during the measurement. We expect to observe such a situation because of our previous flow visualization experiments wherein we showed a pulsating motion of the inner rotating cylinder with time above the critical shear stress. In a shear rate controlled experiment such

situation (Fig. 1c) can only occur if there exists wall slip. Furthermore if a situation arises wherein one observes the coexistence of both (radial and vorticity) types of shear bands and if both show spatio-temporal oscillations then the velocity profile for such a situation would resemble Figure 1d.

Even though extensive investigations [6,7,13,25,26] have been carried out to analyze the microstructures and the resulting viscosities in the vorticity bands formed in a solution of 40 mM CPyCl-NaSal, the system was never studied for the presence or absence of radial or velocity gradient bands. Our goal here is to identify the type of shear bands and to obtain an idea about the local dynamics within each band. We perform the local velocity measurements in the 1 mm gap of the Couette geometry using the UVP method. Experiments in both controlled shear stress and shear rate conditions are described and discussed. The pointwise local velocity measurements are used to identify the flow inside the gap of the Couette cell. In the shear-thickening regime, we observe radial shear bands with a high shear rate band ($\dot{\gamma}_1$) at the rotating wall and a low shear rate band ($\dot{\gamma}_2$) at the stationary wall of the Couette shear cell. With the help of very rapid data aquisition, fast UVP measurements were performed to capture the temporal behavior of the local shear rates. Analyzing the oscillating shear rates in each radial band and comparing the frequency of oscillation to that of the flip-flop behavior of vorticity bands, we show that there is a coexistence of both radial and vorticity bands in this system.

The manuscript is organized as follows: In Section 2 the materials and experimental setup are discussed briefly. Results for both stress-controlled and strain-controlled rheo-UVP experiments are presented and discussed in Section 3 before presenting a summary of the investigations in the forth Section.
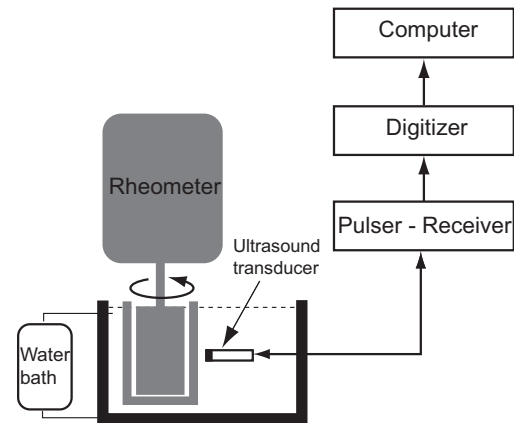
2 Experimental

2.1 Materials

Cetylpyridiunum chloride (CPyCl) and sodium salicylate (NaSal) were obtained from Fluka (Buchs, Switzerland) and used without further purification. A solution of CPyCl-NaSal in water is usally transparent to ultrasonic waves. Thus, in order to measure the velocity profiles, 1 wt% hollow glass spheres (Sphericel, Potters Industries) were added as tracer particles. Required amount of CPyCl to prepare a 40 mM solution was first weighed and dissolved in Millipore water. Then, the glass spheres of mean diameter 10 μm were added to this solution. Once these spheres are homogeneously dispersed in water, NaSal was slowly added. This helps to slowly build-up the viscosity in the sample due to the growth of wormlike micelles in the presence of dispersed glass spheres.

2.2 UVP - Experimental set-up

Simultaneous rheology and local velocity data are measured in a stress-controlled rheometer (TA Instruments
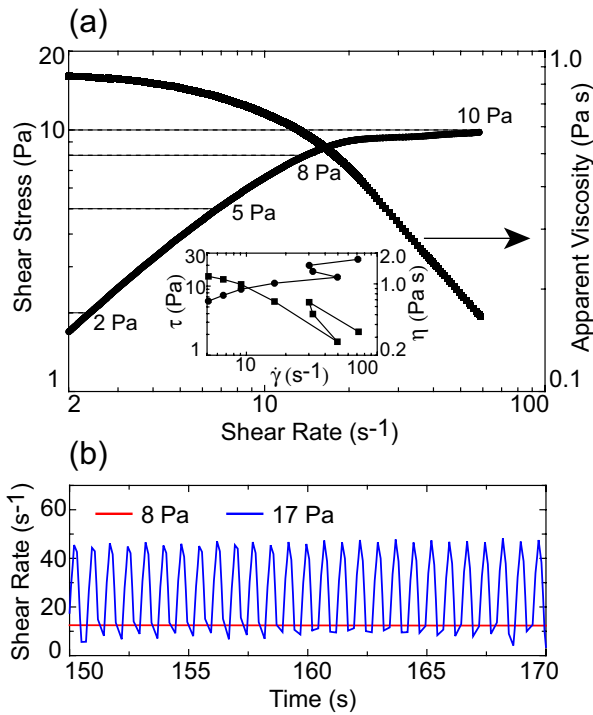

Fig. 2. Ultrasound velocity profiling (UVP) experimental set-up. Figure adapted from Manneville *et al.* [36].

AR 1000), equipped with a transparent Couette geometry. The Couette cell was made of smooth Plexiglas with inner cylinder radius of 24 mm, gap 1 mm and height 30 mm. This whole cell is surrounded by circulated water whose temperature was kept constant at 21 °C. Figure 2 shows a schematic of the UVP experimental set-up. A PVDF piezo-polymer transducer (Panametrics PI 50-2) immersed in the water in front of the stator generates focussed ultrasonic pulses of central frequency $f = 36$ MHz. The transducer is controlled by a pulser-receiver unit (Panametrics 5900PR). Ultrasonic pulses travel through the 1 mm gap of the Couette geometry and are scattered by glass spheres. Backscattered signals are then collected and stored on a high-speed PCI digitizer (Acqiris DP235), and transfered to the host computer for post processing. The spatial resolution of the experimental set-up is of the order of 40 μm and the temporal resolution ranges between 0.02 and 2 s per profile. Details of the experimental set-up, calibration procedure, and data analysis can be found in Manneville *et al.* [36].

3 Results and discussion

3.1 Stress-controlled rheology

Figure 3a displays the flow curve of the surfactant solution seeded with 1 wt% glass spheres. The overall nature of the flow curve did not change with addition of the particles, however the critical stress, τ_c, where the solution exhibits shear-thickening behavior is found to be 10 Pa as compared to 13 Pa observed for a tracer particle free solution. As described previously, when increasing the shear stress, the solution exhibits Newtonian, shear-thinning and shear-thickening behaviors [5,25,26]. For reasons of clarity, the shear-thickening regime is not shown in the main figure, but the inset shows the entire flow curve including the shear-thickening regime. The viscosity drops drastically between 8 and 10 Pa and it is between these shear stresses that a quasi-horizontal stress plateau is observed (Fig. 3a). In comparison to the unseeded solution (see [25]) the shear-thinning plateau is covering a wider
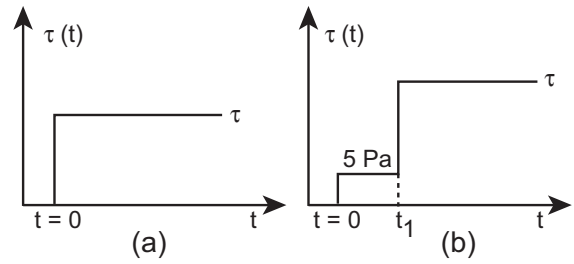
Fig. 4. Rheological test sequence used to measure velocity profiles. (a) Step stress method for shear stresses $\tau \leqslant 10\,\mathrm{Pa}$ and (b) pre-shear and step stress method for shear stresses $\tau > 10\,\mathrm{Pa}$; $t_1 = 40\,\mathrm{s}$.

Fig. 3. (Color online) (a) Flow curve of $40\,\mathrm{mM}$ CPyCl-NaSal solution ($1 < \tau < 10\,\mathrm{Pa}$) with 1 wt% tracer particles recorded under controlled shear stress conditions. The inset shows the full flow curve including the shear-thickening region. Horizontal dashed lines represent the stresses where the steady-state UVP velocity profiles were recorded. (b) Transient shear rate signals below (8 Pa) and above (17 Pa) shear-thickening regime of flow.

range of shear rates. Such a plateau in τ *versus* $\dot{\gamma}$ has been associated to shear-induced transitions or formation of shear-induced structures (SIS) [1,37–40] and studied in the framework of shear banding theories [18,41,42]. Further shearing the sample above the critical shear stress ($\tau_c = 10\,\mathrm{Pa}$), the solution exhibits shear-thickening behavior (inset in Fig. 3a) and this region extends up to $\tau = 17\,\mathrm{Pa}$ as compared to $25\,\mathrm{Pa}$ in the case of the unseeded sample. In this regime of flow, strong temporal oscillations in apparent viscosity and shear rate as well as the flip-flop–like axial motion of the vorticity bands has previously been observed which correspond to fast structural changes in the system [5,25,26]. Figure 3b shows the variation of shear rate as a function of time at 8 and 17 Pa. The shear rate is constant for 8 Pa which is below the shear-thickening regime. However in the shear-thickening regime that follows (*i.e.*, at 17 Pa), the shear rate signal shows large temporal oscillations around a mean value with a characteristic frequency. To investigate the structural transitions in these regimes of flow (shear-thinning and shear-thickening) and to get an idea about the local velocities in shear bands, pointwise local velocity measurements are carried out inside the gap of a Couette cell.

3.2 Rheology and UVP measurements ($\tau \leqslant 10\,\mathrm{Pa}$)

To begin with, several shear stresses below $\tau_c = 10\,\mathrm{Pa}$ are chosen to measure the velocity profiles (dashed lines in
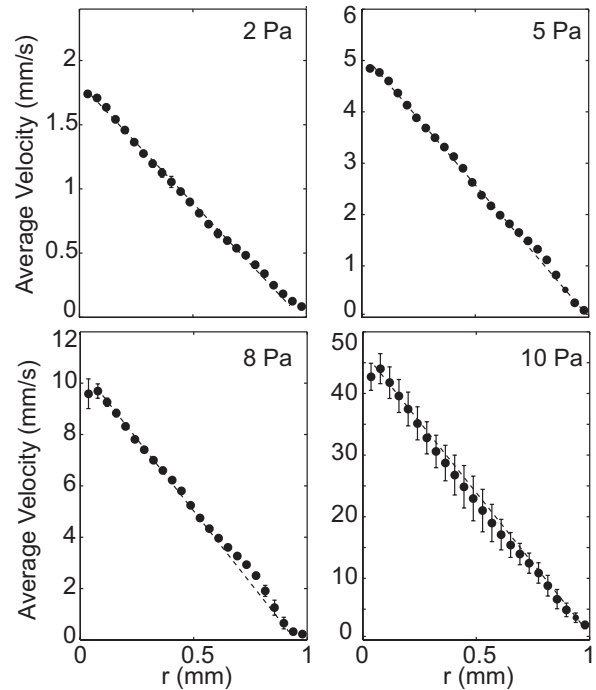
Fig. 5. Time-averaged velocity profiles for different shear stresses in the Newtonian and shear-thinning regime measured in the stress-controlled mode. Error bars correspond to the standard deviation of the local velocities and mainly account for temporal fluctuations in the velocity. r denotes the radial distance to the rotor; $r = 0$ at the rotor and $r = 1$ at the stator.

Fig. 3). Figure 4a shows the rheological protocol used to measure such profiles. At $t = 0$, a shear stress of τ is instantly applied and the velocity profiles are recorded for a minimum of $200\,\mathrm{s}$. These are then averaged and such time-averaged velocity profiles are shown in Figure 5 for different shear stresses. r denotes the radial distance in the gap of the Couette shear cell ($r = 0$ at the rotor and $r = 1$ at the stator). For $\tau = 2\,\mathrm{Pa}$, the profile is very close to a straight line, consistent with the Newtonian behavior of the micellar solution at low shear stresses. However, for $\tau = 10$, the data do not exactly fall on the Newtonian velocity profile but deviates slightly. Such a curvature in the velocity profile is due to the sharp shear-thinning effect [43] observed at $\tau = 10$ but the overall flow behavior of

the solution in 1 mm gap of the shear cell is homogeneous. Furthermore, temporal fluctuations of velocity come in to play at this shear stress. These temporal fluctuations in the measured velocity profiles are due to oscillations in apparent viscosity which start to appear at this critical shear stress ($\tau_c = 10$ Pa).

In most of the experimental works dealing with surfactant systems, it has been argued that a strong *flow-structure* coupling induces new organizations like nematic phases or onion textures or other flow-induced phenomena [14,44–47]. With the evolution of these new structures, the systems exhibit a stress plateau in steady-state flow curve (τ *vs.* $\dot{\gamma}$), which in the case of present seeded material would be $\tau_c = 10$ Pa. Under such flow conditions it is believed that the sheared fluid separates into two differently sheared regions and such a behavior is termed as shear-banding flow. In a Couette shear cell under shear-banding situation, one observes a highly sheared band near the rotating cylinder and a weakly sheared band at the stationary wall. Those systems exhibiting stress plateau behavior have been investigated by ultrasound velocimetry [23,24,48], flow bire-fringence [40], small-angle neutron scattering [49], particle image velocimetry (PIV) [50,51] and NMR velocity measurements [52], and an inhomogeneous flow in the gap of the Couette cell has indeed been observed with the presence of high and low shear bands. Since such an inhomogeneous flow behavior has been experimentally observed in many surfactant systems, the presence of a stress plateau is considered as the hallmark of shear-banding flows (see Fig. 1b). This generality has motivated many recent theoretical works involving phenomenological models as well as microscopic approaches [29,53–55]. In our case, rheologically, a quasi-horizontal stress plateau is indeed observed between $\tau = 8$ and 10 Pa. However, we have to mention here that we did not observe any inhomogeneous flow in the plateau region.

3.3 Transient UVP measurements ($\tau > 10$ Pa)

3.3.1 Time-averaged velocity profiles

As shown in the inset of Figure 3, the solution shows shear-thickening behavior above 10 Pa. Previous study of the system showed formation of alternating vorticity bands in this flow regime with oscillations in the apparent viscosity and shear rate [25,26]. Hence one expects a rich variety of time-dependent phenomena, such as large temporal oscillations of the velocity in the shear-thickening regime. To investigate these fast time-dependent behaviors, careful rheological protocols should be used while measuring the velocity in the annular gap. Figure 4b shows such an experimental protocol used to measure transient velocity profiles. A step stress of 5 Pa is applied at time $t = 0$ and the solution is pre-sheared for 40 s at this shear stress. Then the sample is subjected to a higher stress ($\tau > \tau_c$) for more than 1000 s and in this time period transient velocity profiles are recorded at a rate of 20 profiles per
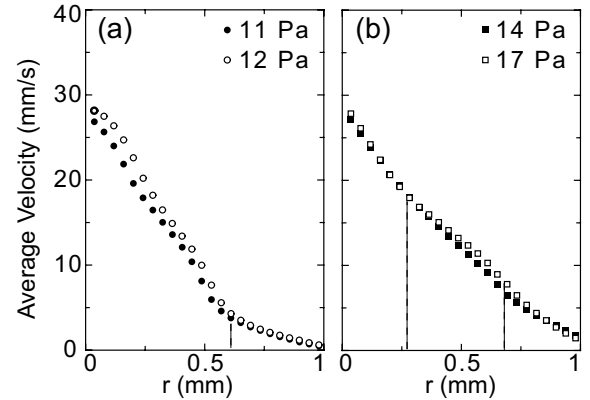
Fig. 6. Time-averaged velocity profiles for different shear stresses in the shear-thickening regime measured in the stress-controlled mode. r denotes the radial distance to the rotor; $r = 0$ at the rotor and $r = 1$ at the stator. Dashed vertical lines indicate the position of the interface between the radial bands.

second. Such very fast measurements help us to capture fast dynamics in this system.

The velocity profiles measured above the critical shear stress, *i.e.*, at 11, 12, 14 and 17 Pa, show large temporal fluctuations which might correspond to the flip-flop–like motion of the vorticity bands. Figure 6 shows *time-averaged* velocity profiles for the above-mentioned shear stresses in the shear-thickening region. Typically more than 200 profiles have been averaged to obtain this data. The standard deviation is not shown in this figure for reasons of clarity but it will be discussed in the next section. Measurements above 17 Pa could not be performed due to stronger viscoelastic effects (rod-climbing). Figure 6a shows the average velocity profiles measured for 11 and 12 Pa close to τ_c and Figure 6b shows the same for 14 and 17 Pa further away from τ_c. Compared to the velocity profiles of Figure 5 ($\tau \leqslant \tau_c$), these profiles clearly reveal an inhomogeneous flow with an unambiguous radial banding structure. For shear stresses close to τ_c (Fig. 6a), two shear bands coexist in the 1 mm gap of the Couette geometry with the interface of the bands located approximately at $r \simeq 0.6$ mm. This is in accordance to the classical picture of shear-banding flow, with a highly sheared band located at the rotor accompanied by a low shear band near the stator [8,23,40,46,47,52,56] and adds another complexity to the rheological response function of the shear-thickening 40 mM CPyCl-NaSal wormlike micellar solution: Until now only vorticity bands were found for this system ($\tau \geqslant \tau_c$) while local velocimetry now clearly shows additionally radial banding in the shear-thickening regime.

Velocity profiles in Figure 6a present only a single interface whereas three differently sheared regions (different slopes in the velocity profile) can be seen for shear stresses $\tau = 14$ and 17 Pa as displayed in Figure 6b. This indicates the presence of three shear bands in the annular gap. Furthermore, at these stresses the flow becomes very complex with large fluctuations in the velocity. These temporal fluctuations will be discussed in the next section. We

have to mention here that the three banded situation appears only momentarily for $\tau = 14$ Pa but the third band becomes more pronounced with increase in the shear stress ($\tau = 17$ Pa). As mentioned above the interface between the radial bands remains approximately at $r = 0.6$ mm and it is very interesting to see that when increasing the shear stress from 11 to 17 Pa, the *average* position of the interface, δ, does not move towards the stator as observed by other authors [8,41,46,47]. Furthermore, the development of the radial bands is as described in the literature, which is by nucleation and growth mechanism. Start up measurements between $t_1 < t < t_1 + 10$ s (data not shown) showed that a high shear band nucleates at the inner wall and grows rapidly towards the stator before stabilizing approximately at $\delta \simeq 0.6$ mm. This mechanism of nucleation and growth is very rapid as compared to other systems wherein it can take few minutes to achieve a stable interface. In all cases ($\tau = 11$ to 17 Pa), the flow presents large fluctuations of the velocity in each band with oscillating interface and even in the time domain $t_1 < t < t_1 + 10$ s, the average position of the interface fluctuates continuously.

### 3.3.2 Temporal evolution of local shear rates and interface dynamics

As mentioned above, large temporal fluctuations in the local velocity are observed in each band in particular when the critical shear stress is overcome. Assuming no wall slip, if $v_1(t)$ denotes the rotor velocity, $\delta(t)$ the position of the interface, and $v(\delta(t), t)$ the velocity at the interface, then the local shear rates in the weakly sheared band, $\dot{\gamma}_2$, and in the high shear band, $\dot{\gamma}_1$, can be calculated using the following equations [47]:

$$\dot{\gamma}_2 = \frac{(R_1 + \delta)^2 + R_2^2}{(R_1 + \delta)(R_1 + R_2 + \delta)} \cdot \frac{v(\delta)}{(e - \delta)}, \tag{1}$$

$$\dot{\gamma}_1 = \frac{(R_1 + \delta)^2 + R_1^2}{R_1(2R_1 + \delta)} \cdot \frac{v_1 - \frac{R_1}{R_1 + \delta} \cdot v(\delta)}{\delta}, \tag{2}$$

where R_1 and R_2 are the inner and outer radii of the Couette geometry and $e = (R_2 - R_1)$.

Figure 7 shows the evolution of local shear rates and the position of the interface as a function of time for applied shear stresses $\tau = 11$, 12 Pa. Because of the fluctuations in the local velocities, one observes oscillations in the local shear rates ($\dot{\gamma}_1, \dot{\gamma}_2$) in each band. A closer look at these oscillations shows that $\dot{\gamma}_1$ and $\dot{\gamma}_2$ are anti-correlated but $\delta(t)$ seems to be in phase with $\dot{\gamma}_2$ (at least better correlated than to $\dot{\gamma}_1$). The position of the interface between the two bands also oscillates around a mean value of $\delta \simeq 0.6$ mm. Figure 8 displays similar results for $\tau = 14$ Pa. Here we show the temporal oscillations in only two bands as the third band was appearing at irregular intervals. The oscillations in $\dot{\gamma}_1$ and $\dot{\gamma}_2$ for $\tau = 14$ Pa are not as regular as for $\tau = 11$ and 12 Pa (Fig. 7) and also the amplitude of the oscillations in $\delta(t)$ for $\tau = 14$ Pa is larger than in Figure 7 ($\tau = 11$, 12 Pa). Furthermore, in the case of $\tau = 14$ Pa, the relative fluctuations of the interface position is about 22% as compared to 10% for 11
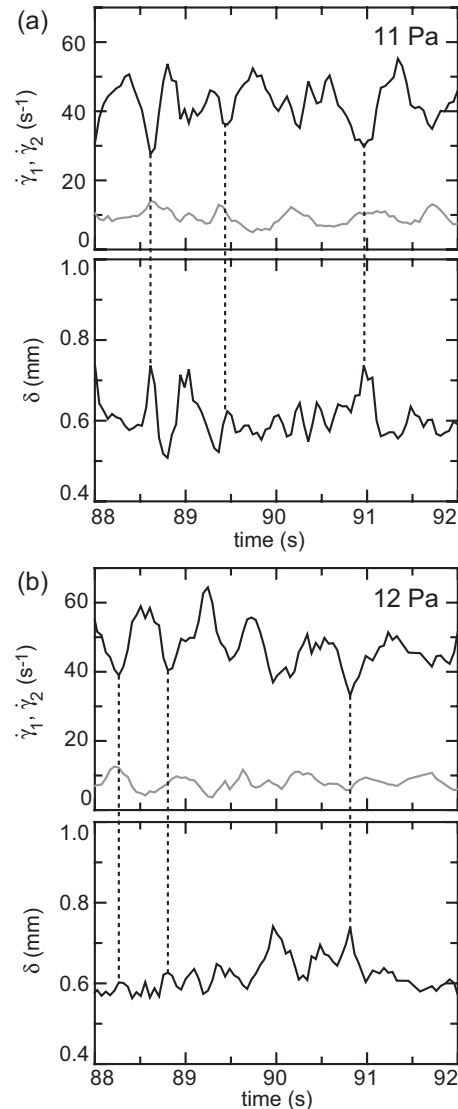
Fig. 7. Local shear rates ($\dot{\gamma}_1, \dot{\gamma}_2$) and position of the interface (δ) as a function of time for (a) 11 Pa and (b) 12 Pa. The black and the gray lines on the top section of each figure correspond, respectively, to the highly sheared band ($\dot{\gamma}_1$) near the rotor and to the weakly sheared band ($\dot{\gamma}_2$) near the stator.
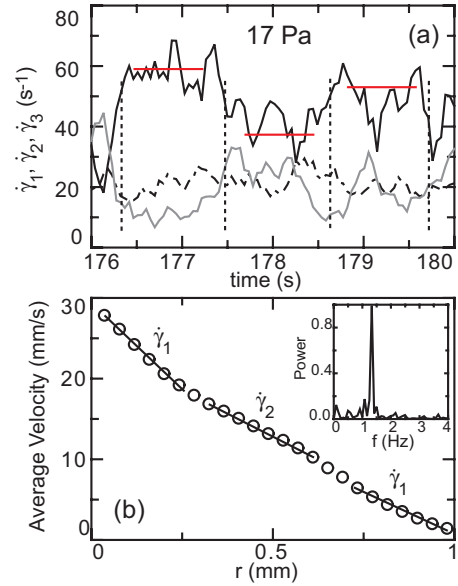
and 12 Pa. It is quite clear that an increase in shear stress causes larger fluctuations in the local velocity and also in the interface position. The presence of two or three radial bands, the anti-correlated behavior of local shear rates, the fluctuations in the interface position, as well as the overall transient oscillations in the signals indicate that velocity and vorticity bands are superimposed. This point is further supported in Figure 9a, which shows the local shear rates for $\tau = 17$ Pa. Here, instead of two bands, we clearly see a situation with three individual shear rates $\dot{\gamma}_1$, $\dot{\gamma}_2$, and $\dot{\gamma}_3$, while it becomes difficult to figure out the exact positions of the interface. Similar to Figure 7, ($\tau = 11$, 12 Pa) the highly sheared band, $\dot{\gamma}_1$, and weakly sheared band, $\dot{\gamma}_3$, are anti-correlated. However there is no obvious correlation between the third band in the middle and the two other bands. At certain time intervals the local shear
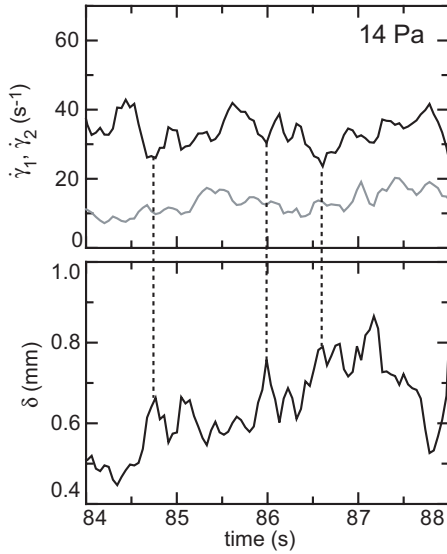
Fig. 8. Local shear rates ($\dot{\gamma}_1$, $\dot{\gamma}_2$) and position of the interface (δ) as a function of time for a shear stress of 14 Pa. The black and the gray lines on the top part of the figure correspond, respectively, to the highly sheared band ($\dot{\gamma}_1$) near the rotor and to the weakly sheared band ($\dot{\gamma}_2$) near the stator.

Fig. 9. (a) Local shear rates ($\dot{\gamma}_1$, $\dot{\gamma}_2$, $\dot{\gamma}_3$) as a function of time for a shear stress of 17 Pa. The black line corresponds to the highly sheared band ($\dot{\gamma}_1$) near the rotor, the dashed line to the shear band in the middle ($\dot{\gamma}_2$) and the gray line corresponds to the weakly sheared band ($\dot{\gamma}_3$) near the stator. (b) Time-averaged velocity profile as shown in Figure 6b indicating the regions used to fit the velocity profiles to obtain the local shear rates. The insert in (b) shows the FT power spectrum.

rates in all the three bands are equal and the flow seems to be homogeneous (see for 178 s in Fig. 9a). However, such a homogeneous flow is very short lived (not more than 1 s) and three-band scenario appears again. Horizontal lines in Figure 9a indicate regions where the shear rate $\dot{\gamma}_1$ is at different transient velocity levels and are anti-correlated to $\dot{\gamma}_3$. Furthermore, Figure 9b shows the time-averaged regions of the corresponding three-banded velocity profiles which are used to calculate all three local shear rates ($\dot{\gamma}_1$, $\dot{\gamma}_2$, and $\dot{\gamma}_3$).

As proposed in Figure 1c we expected to observe a clear difference in the velocity profiles of the alternating vorticity bands. However, the Rheo-UVP experiments indicate an additional feature of radial banding and no direct identification of the vorticity bands. We propose that the temporal oscillations observed in the local shear rates are due to the flip-flop–like axial motion of the vorticity bands and the anti-correlation between the shear rates is the microscopic manifestation of this flip-flop motion or in other words of the different viscosity in the bands. In Figure 9a horizontal lines give a rough estimate of the presence of vorticity bands with different shear rates, *i.e.*, viscosity and the transient nature of the bands at the position of the UVP sensor. Beside the different levels, the flip-flop motion of the vorticity bands is also captured by the length of the lines indicating that the different banded states exist about 0.6 s, *i.e.*, having a frequency of about 1.5 to 2 Hz. It is known from previous investigations that the flip-flop–like motion depends on gap size and applied shear stress [25,26]. For the Couette geometry used here, a temporal change of band structure within roughly half-second is excepted. Indeed by analysing the oscillating shear rate signals (both, $\dot{\gamma}_1$, $\dot{\gamma}_2$) using FFT power spectrum analysis, as shown in the insert of Figure 9b, we
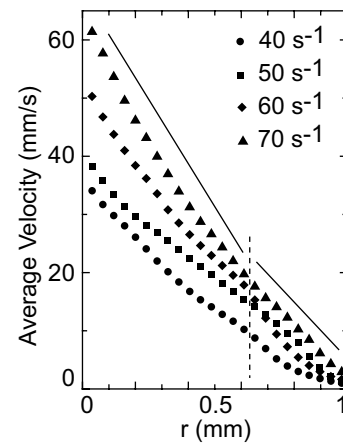
obtain an average frequency of approximately 1.5 Hz or a period of 0.6 s. The frequency is in the same range as we observed for the appearance and disappearance of the vorticity bands in optical experiments [26]. Although the velocity signal is extremely noisy and therefore frequency analysis is not as accurate as in the case of our previous work [25,26], we postulate a banding situation as depicted in Figure 1d where radial and vorticity bands coexist. This confirms the presence of alternating vorticity bands and unambiguously shows the coexistence of both radial and vorticity bands in the gap. Here the different slopes of the velocity profiles and consequently the different values of the viscosities would fluctuate not only in the magnitude of the velocity but also in the position of the boundary. A velocity difference resulting in the different viscosities must be generated by a different slope of the individual radial bands of each vorticity band and, as a consequence, the oscillatory motion of the rotating cylinder. Due to the addition of glass spheres (seeding for UVP), the whole sample becomes turbid (milky) and hence a simultaneous optical observation of transparent or turbid bands with the UVP experiments was not possible. Alternative measures such as investigation using two ultrasonic transducers positioned at different heights of the Couette cell have to be taken to access the information about the presence or absence of vorticity bands.

In the recent theoretical work by Fielding [35], the author depicts the scenario of vorticity banding or vorticity rolls using a diffusive Johnson-Segalman model. The model predicts that vorticity structuring in complex
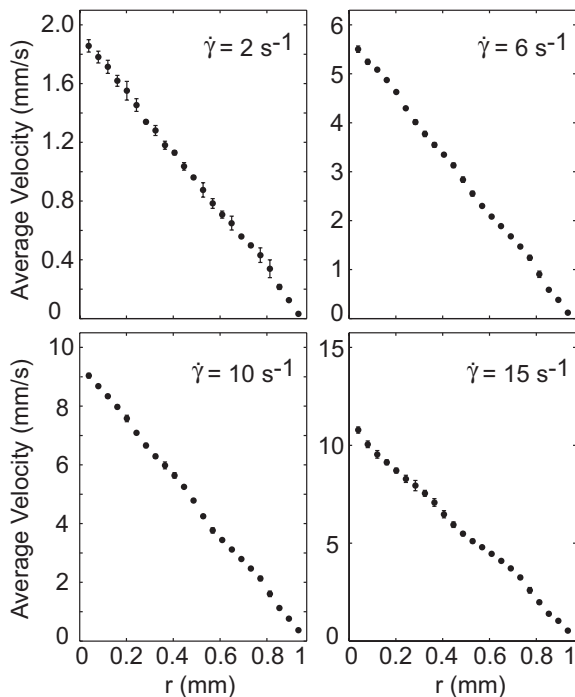
Fig. 10. Time-averaged velocity profiles for different shear rates in the Newtonian (2 and $6\,\mathrm{s}^{-1}$) and shear-thinning (10 and $15\,\mathrm{s}^{-1}$) regimes measured in the strain-controlled mode. Error bars correspond to the standard deviation of the local velocities and mainly account for temporal fluctuations in the velocity. r denotes the radial distance to the rotor; $r = 0$ at the rotor and $r = 1$ at the stator.

Fig. 11. Time-averaged velocity profiles for different shear rates in the shear-thickening regime measured in the strain-controlled mode. The dashed vertical line indicates the position of the interface between the radial bands and the solid lines are guides to the eye. r denotes the radial distance to the rotor; $r = 0$ at the rotor and $r = 1$ at the stator.

fluids can be triggered by the linear instability of one-dimensional gradient shear banding. The experimental results presented here using fast UVP measurements show some evidence where this model may be relevant. The velocity profiles across the gap of the rheometer in the shear-thickening regime (Fig. 6) show that our system first develops radial bands with the interface of the bands being at $0.6\,\mathrm{mm}$ from the moving wall, and then within a short induction time of a few seconds vorticity bands appear, which we observe as regular oscillations in the local shear rate. These oscillations in the local shear rate become more pronounced with increased shear stress ($\tau \geqslant 14\,\mathrm{Pa}$) indicating the formation of fully developed vorticity bands. During flow visualization studies using a camera mounted below the transparent bottom of the Couette shear cell we observed the turbidity being first developed at the rotating wall (for all shear stresses in the shear-thickening regime, *i.e.*, $\tau \geqslant 11\,\mathrm{Pa}$) and a few seconds later macroscopic vorticity bands appear. Similar oscillations in the velocity profiles were measured by Decruppe [8] for cetyltrimethylammonium bromide (CTAB)-NaSal system in the narrow shear-thickening region $6.5 \leqslant \dot{\gamma} \leqslant 7.5\,\mathrm{s}^{-1}$, *i.e.*, at the end of the stress plateau regime. The authors particularly observed a monotonous variation of the velocity in the gap along with very large fluctuations of the local velocity. Comparing our work to the system studied by Decruppe, we believe that a similar situation (coexistence of radial and vorticity bands) may be existing in

their systems as well. With the emergence of the recent theoretical [35] and experimental work, it becomes necessary to perform sophisticated (fast) flow visualization experiments to shed more light on the phenomena of gradient shear banding triggering the vorticity structring in complex fluids.

3.4 Strain-controlled experiments

In this section, we very briefly report on the local velocity measurements carried out in the strain-controlled mode of the rheometer. Similar to the experiments in the earlier section the measurements are carried out in the Newtonian, shear-thinning (stress plateau) and shear-thickening flow regime. As shown in Figure 10, the flow is homogeneous in the Newtonian and shear-thinning flow regions ($\dot{\gamma} \leqslant 15\,\mathrm{s}^{-1}$). However, the velocity profile is somewhat inhomogeneous in the shear-thickening regime ($15\,\mathrm{s}^{-1} \leqslant \dot{\gamma} \leqslant 70\,\mathrm{s}^{-1}$) as depicted in Figure 11. But, the pronounced two-banded situation that was observed in stress-controlled experiments (Fig. 6) is not seen in shear rate controlled measurements. It seems that either the flow is almost homogeneous or chaotic in the shear rate controlled mode. Moreover, in shear rate controlled experiments wall slip is sometimes detected at the rotating wall for a shear rate of $15\,\mathrm{s}^{-1}$ and such wall slip persists till about only $20\,\mathrm{s}^{-1}$. However, with our measurements in the Couette shear cell we did not observe a systematic wall slip and hence it is difficult to relate the slip phenomena to the observed shear banding flow.

4 Summary

In this study we have described and discussed local velocity measurements performed using ultrasonic velocimetry on an equimolar ($40\,\mathrm{mM}$) cetylpyridinium chloride-sodium

salicylate mixture forming wormlike micelles. When the shear stress is increased the solution exhibits Newtonian, shear-thinning and shear-thickening behavior, respectively. In the shear-thickening regime, transparent and turbid bands appear in the vorticity direction of the Couette geometry. These vorticity bands alternate in their position (flip-flop), forcing the free parameter (shear rate, $\dot{\gamma}$, apparent viscosity, η) to oscillate under controlled shear stress conditions. Pointwise local velocity measurements using high-frequency ultrasonic velocimetry revealed a homogeneous flow inside the gap of the Couette cell in the stress plateau region. However, when the solution is sheared beyond the critical shear stress (shear-thickening regime), a two-banded situation appears in the gap of the Couette cell showing the presence of a highly sheared band ($\dot{\gamma}_1$) at the rotating wall and a weakly sheared band ($\dot{\gamma}_2$) at the stationary wall. When further increasing the shear stress, the flow inside the gap becomes even more complex with the presence of more than two radial shear bands. To investigate the complex flow behavior in the shear-thickening regime, we performed, with the help of very rapid data aquisition, fast UVP measurements to capture the interface dynamics and the temporal behavior of the local shear rates. Such measurements indicated a very complex time-dependent flow behavior with large temporal oscillations in the velocity profile. The frequency of the oscillations in the velocity profiles corresponded to that of appearance and disappearance of vorticity bands at the position of the UVP sensor. This gives an indication for the coexistence of both radial and vorticity banding in this system. Furthermore, the UVP measurements performed under shear rate controlled mode of the rheometer did not show significant radial shear banding behavior in the shear-thickening flow region. We are currently in the process of investigating the presence of coexisting vorticity and radial bands with a sub-structure in the radial bands by direct birefringence measurements. Preliminary birefringence results show different local material stages within the radial bands under non-monotonic flow conditions. To address the spatial-transient correlation we will also perform UVP experiments simultaneously at two different heights of the Couette shear cell using two ultrasonic transducers to obtain position and timing of the vorticity banding.

References

1. H. Rehage, H. Hoffmann, Mol. Phys. **74**, 933 (1991).
2. C. Grand, J. Arrault, M.E. Cates, J. Phys. II **7**, 1071 (1997).
3. T. Shikata, H. Hirata, T. Kotaka, Langmuir **3**, 1081 (1987).
4. A.M. Wunderlich, P.O. Brunn, Colloid Polym. Sci. **267**, 627 (1989).
5. P. Fischer, Rheol. Acta **39**, 234 (2000).
6. E.K. Wheeler, P. Fischer, G.G. Fuller, J. Non-Newtonian Fluid Mech. **75**, 193 (1998).
7. B.M. Marin-Santibanez, J. Perez-Gonzalez, L. de Vargas, F. Rodriguez-Gonzalez, G. Huelsz, Langmuir **22**, 4015 (2006).
8. J.P. Decruppe, O. Greffier, S. Manneville, S. Lerouge, Phys. Rev. E **73**, 061509 (2006).
9. B.A. Schubert, N.J. Wagner, E.W. Kaler, S.R. Raghavan, Langmuir **20**, 3564 (2004).
10. H. Azzouzi, J.P. Decruppe, S. Lerouge, Eur. Phys. J. E **17**, 507 (2005).
11. J.F. Berret, D.C. Roux, G. Porte, P. Lindner, Europhys. Lett. **25**, 521 (1994).
12. P. Boltenhagen, Y.T. Hu, E.F. Matthys, D.J. Pine, Phys. Rev. Lett. **79**, 2359 (1997).
13. P. Fischer, E.K. Wheeler, G.G. Fuller, Rheol. Acta **41**, 35 (2002).
14. I.A. Kadoma, J.W. van Egmond, Phys. Rev. Lett. **80**, 5679 (1998).
15. R. Oda, P. Panizza, M. Schmutz, F. Lequeux, Langmuir **13**, 6407 (1997).
16. N.A. Spenley, X.F. Yuan, M.E. Cates, J. Phys. II **6**, 551 (1996).
17. P.D. Olmsted, C.Y.D. Lu, Phys. Rev. E **60**, 4397 (1999).
18. S.M. Fielding, P.D. Olmsted, Eur. Phys. J. E **11**, 65 (2003).
19. V. Schmitt, C.M. Marques, F. Lequeux, Phys. Rev. E **52**, 4009 (1995).
20. J.P. Decruppe, R. Cressely, R. Makhloufi, E. Cappelaere, Colloid Polym. Sci. **273**, 346 (1995).
21. S. Lerouge, J.P. Decruppe, C. Humbert, Phys. Rev. Lett. **81**, 5457 (1998).
22. E. Fischer, P.T. Callaghan, Phys. Rev. E **64**, 011501 (2001).
23. L. Becu, S. Manneville, A. Colin, Phys. Rev. Lett. **93**, 018301 (2004).
24. S. Manneville, J.B. Salmon, L. Becu, A. Colin, F. Molino, Rheol. Acta **43**, 408 (2004).
25. V. Herle, P. Fischer, E.J. Windhab, Langmuir **21**, 9051 (2005).
26. V. Herle, J. Kohlbrecher, B. Pfister, P. Fischer, E.J. Windhab, Phys. Rev. Lett. **99**, 158302 (2007).
27. P. Hu, Y.T. Boltenhagen, D.J. Pine, J. Rheol. **42**, 1185 (1998).
28. L. Hilliou, D. Vlassopoulos, Ind. Eng. Chem. Res. **41**, 6246 (2002).
29. S.M. Fielding, P.D. Olmsted, Phys. Rev. Lett. **92**, 084502 (2004).
30. R. Ganapathy, A.K. Sood, Phys. Rev. Lett. **96**, 108301 (2006).
31. M.E. Cates, S.M. Fielding, Adv. Phys. **55**, 799 (2006).
32. J.L. Goveas, D.J. Pine, Europhys. Lett. **48**, 706 (1999).
33. M.E. Cates, S.J. Candau, Europhys. Lett. **55**, 887 (2001).
34. A. Aradian, M.E. Cates, Europhys. Lett. **70**, 397 (2005).
35. S.M. Fielding, Phys. Rev. E **76**, 016311 (2007).
36. S. Manneville, L. Becu, A. Colin, Eur. Phys. J. Appl. Phys. **28**, 361 (2004).
37. J.F. Berret, Langmuir **13**, 2227 (1997).
38. J.F. Berret, G. Porte, J.P. Decruppe, Phys. Rev. E **55**, 1668 (1997).
39. J.I. Escalante, E.R. Macias, F. Bautista, J.H. Perez-Lopez, J.F.A. Soltero, J.E. Puig, O. Manero, Langmuir **19**, 6620 (2003).
40. J.P. Decruppe, S. Lerouge, J.F. Berret, Phys. Rev. E **63**, 022501 (2001).
41. N.A. Spenley, M.E. Cates, T.C.B. McLeish, Phys. Rev. Lett. **71**, 939 (1993).
42. F. Bautista, J.F.A. Soltero, E.R. Macias, J.E. Puig, O. Manero, J. Phys. Chem. B **106**, 13018 (2002).

43. J.B. Salmon, A. Colin, S. Manneville, F. Molino, Phys. Rev. Lett. **90**, 228303 (2003).
44. J.F. Berret, D.C. Roux, G. Porte, J. Phys. II **4**, 1261 (1994).
45. J.F. Berret, R. Gamez-Corrales, J. Oberdisse, L.M. Walker, P. Lindner, Europhys. Lett. **41**, 677 (1998).
46. J.B. Salmon, S. Manneville, A. Colin, Phys. Rev. E **68**, 051503 (2003).
47. S. Manneville, J.B. Salmon, A. Colin, Eur. Phys. J. E **13**, 197 (2004).
48. J.B. Salmon, A. Colin, D. Roux, Phys. Rev. E **66**, 031505 (2002).
49. E. Cappelaere, J.F. Berret, J.P. Decruppe, R. Cressely, P. Lindner, Phys. Rev. E **56**, 1869 (1997).
50. A.F. Mendez-Sanchez, M.R. Lopez-Gonzalez, V.H. Rolon-Garrido, J. Perez-Gonzalez, L. de Vargas, Rheol. Acta **42**, 56 (2003).
51. A.F. Mendez-Sanchez, J. Perez-Gonzalez, L. de Vargas, J.R. Castrejon-Pita, A.A. Castrejon-Pita, G. Huelsz, J. Rheol. **47**, 1455 (2003).
52. M.M. Britton, R.W. Mair, R.K. Lambert, P.T. Callaghan, J. Rheol. **43**, 897 (1999).
53. G. Picard, A. Ajdari, L. Bocquet, F. Lequeux, Phys. Rev. E **66**, 051501 (2002).
54. J.K.G. Dhont, Phys. Rev. E **60**, 4534 (1999).
55. P.D. Olmsted, P. Goldbart, Phys. Rev. A **41**, 4578 (1990).
56. E. Fischer, P.T. Callaghan, Europhys. Lett. **50**, 803 (2000).